Grain Level Dwell Fatigue Crack Nucleation Model for Ti Alloys Using Crystal Plasticity Finite Element Analysis

Kedar Kirane
Graduate Research Associate

Somnath Ghosh[1]
Nordholt Professor
e-mail: ghosh.5@osu.edu

Mike Groeber
Graduate Research Associate

Amit Bhattacharjee[2]
Postdoctoral Research Scholar

Computational Mechanics Research Laboratory,
Department of Mechanical Engineering,
The Ohio State University,
Columbus, OH 43210

A microstructure sensitive criterion for dwell fatigue crack initiation in polycrystalline alloy Ti-6242 is proposed in this paper. Local stress peaks due to load shedding from time dependent plastic deformation fields in neighboring grains are held responsible for crack initiation in dwell fatigue. An accurately calibrated and experimentally validated crystal plasticity finite element (FE) model is employed for predicting slip system level stresses and strains. Vital microstructural features related to the grain morphology and crystallographic orientations are accounted for in the FE model by construction of microstructures that are statistically equivalent to those observed in orientation imaging microscopy scans. The output of the finite element method model is used to evaluate the crack initiation condition in the postprocessing stage. The functional form of the criterion is motivated from the similarities in the stress fields and crack evolution criteria ahead of a crack tip and dislocation pileup. The criterion is calibrated and validated by using experimental data obtained from ultrasonic crack monitoring techniques. It is then used to predict the variation in dwell fatigue lifetime for critical microstructural conditions. The studies are extended to field experiments on β forged Ti-6242. Macroscopic aspects of loading are explored for their effect on dwell fatigue life of Ti-6242.
[DOI: 10.1115/1.3078309]

Keywords: Ti-6242, crack initiation, dwell fatigue, crystal plasticity, sensitivity studies

1 Introduction

The fatigue life cycles of titanium alloys, such as Ti-6242, can vary significantly with different microscopic material parameters and macroscopic loading conditions. For instance, these alloys exhibit significant reduction in life when subjected to dwell fatigue, as compared with a continuous cyclic loading or normal fatigue [1]. This behavior, termed as dwell sensitivity, has received significant research attention in the past and is the focus of the present work. Dwell sensitivity of Ti alloys is attributed to their susceptibility to room temperature creep [2]. During the hold period in each dwell cycle, certain favorably oriented microstructural regions of Ti-6242 undergo significant plastic straining due to slip on favorably oriented slip systems. This results in an increase in the local stress in adjacent unfavorably oriented grains in an attempt to maintain compatibility, a phenomenon known as load shedding [3]. This stress concentration has been found to cause early crack initiation under dwell fatigue in Ref. [4]. Several microstructural and macroscopic factors affect stress evolution due to load shedding, which in turn influences the dwell fatigue life. For instance, a significant reduction in dwell fatigue life of Ti-6242 has been reported in Ref. [5] for a high microtexture, while in Ref. [6] shorter hold times have been seen to improve the same. For a holistic understanding of the dwell fatigue phenomenon, it is necessary to investigate the effect of different microscopic and macroscopic parameters on fatigue life. Such understanding will allow the development of a robust predictive capability that can account for the dependence of dwell fatigue life on these parameters and minimize uncertainties in predictions.

Accurate prediction of the dwell fatigue nucleation in Ti alloys is important especially to the aerospace engine companies for their life prediction and design programs. A number of the existing fatigue analysis methods by, e.g., the stress-life or strain-life approaches, or damage tolerant approaches, are phenomenological in nature. These models show significant scatter in their predictions due to lack of underlying physics based mechanisms and information about the actual material microstructure. They have been largely unsuccessful in predicting the observed variation in dwell fatigue life with microstructural conditions. Also these methods typically require a large number of experiments for generating extensive databases, and are quite expensive. A material microstructure based detailed mechanistic model for fatigue crack nucleation is seen as a promising alternative to such empiricism with a higher probability of accurate fatigue failure prediction. The main objective of this paper is to develop an experimentally validated computational model for load shedding induced dwell fatigue crack initiation in Ti-6242 that accounts for microstructural parameters and their variations.

To build this criterion from finite element (FE) simulations, it is important for the FE model to capture the grain-level morphological details, as well as driving mechanisms of crack initiation at this level. The microstructural response of Ti-6242 is modeled using a size and rate dependent anisotropic elastocrystal plasticity constitutive model developed and experimentally validated in [3,7–9]. Microstructural features such as grain size, grain neighborhood distributions, grain orientations etc are accounted for in a statistically equivalent sense in the model. A method of simulating 3D FE models statistically equivalent to projected 2D orientation microscopy images of the microstructures has been developed in Refs. [10–12]. This is used in this work as a microstructure and FE model builder.

[1]Corresponding author.
[2]Also at Materials Science and Engineering, The Ohio State University.
Contributed by the Materials Division of ASME for publication in the JOURNAL OF ENGINEERING MATERIALS AND TECHNOLOGY. Manuscript received December 31, 2007; final manuscript received November 2, 2008; published online March 6, 2009. Review conducted by Hussein Zbib.

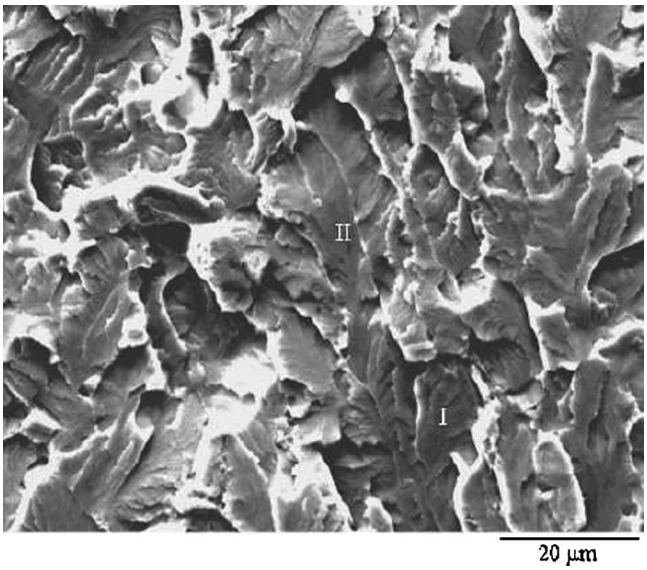

Fig. 1 Fractograph of a faceted initiation site for a failed Ti-6242 dwell fatigue sample

Load shedding causes time dependent local stress concentration near grain boundaries due to dislocation pileup in neighboring grains [13]. The proposed crack nucleation model is motivated by the similarities in the functional forms of the stress fields and crack evolution criteria ahead of a crack tip and dislocation pileup, respectively [14]. The criterion incorporates an effective mixed mode stress acting on a slip plane, defined as a combination of normal and shear stresses to account for mode mixity. It is also necessary to account for the nonlocal effects of the dislocation pileup in the adjacent grain, which results in the incorporation of a nonlocal plastic strain and its gradient. Critical crack initiation parameters are calibrated by comparing results of finite element method (FEM) simulations with experimental observations using ultrasonic monitoring techniques, such as acoustic microscopy. The calibrated crack nucleation criterion is subsequently validated with experimental results on dwell fatigue of Ti-6242 alloy. Sensitivity studies are also conducted to examine the dependence of crack nucleation on critical microstructural parameters. Finally, studies are conducted with fully β-forged microstructure, for which nucleation parameters are calibrated from field experiment data provided by Hall [15]. To accommodate the large number of cycles to failure ($\sim$20,000) in these experiments, a multitime scaling technique that has been developed in Ref. [16] is employed. It is impossible to simulate this many cycles for the polycrystalline microstructure by using a single time scale analysis using conventional FEM. In Sec. 7, macroscopic aspects of loading are explored for their effect on dwell fatigue life of Ti-6242.

2 Load Shedding Phenomenon in Polycrystalline Ti-6242

2.1 Experimental Investigations on Crack Initiation

2.1.1 Fractography and Orientation Imaging Microscopy. Extensive experimental studies on the relation between crack evolution and crystallographic orientations in Ti-6242 have been conducted in Ref. [17] using quantitative tilt fractography and electron back scattered diffraction (EBSD) techniques in scanning electron microscopy (SEM). Figure 1 shows a fractograph of a crack initiation site for a Ti-6242 sample in dwell fatigue, which is found to consist of facets that form on the basal plane of the primary α grains (hcp) lying almost perpendicular to the principal tensile loading direction [4]. It has been observed in Ref. [18] that the angle between the loading axis and the c axis, i.e., the c axis orientation (θ_c) of the grains at the failure site is quite small ($\sim$0–30 deg). Furthermore, the failure site shows a low prism activity with a Schmid factor (SF) $\sim$0–0.1 and a moderate basal activity with a SF$\sim$0.3–0.45. However, the region surrounding the failure site has a high prismatic and basal activity with a SF $=\sim$0.5. Thus, it may be inferred that while crack initiation occurs in a region that is unfavorably oriented for slip, it is surrounded by grains that are favorably oriented for slip. In other words, crack initiates in a hard oriented grain surrounded by soft oriented grains. The observations suggest time dependent accumulation of stress in hard oriented grains due to load shedding with increasing plastic deformation in the surrounding soft grains, which is responsible for crack initiation in alloys like Ti-6242 under creep and dwell loading.

2.1.2 Crack Detection and Monitoring in Mechanical Tests on α/β Forged Ti-6242. Ultrasonic techniques, such as in situ surface acoustic wave techniques, have been developed for monitoring the subsurface phenomenon of crack initiation [3,4], which have been applied to high microtexture α/β forged Ti-6242 samples in Refs. [6,19] for dwell fatigue and creep experiments. Three tests from this set are considered as references here, the microstructures of which are labeled as MS1, MS2, and MS3. Each trapezoidal dwell cycle in these tests had a maximum applied load of 869 MPa (95% of yield stress), a hold time of 2 min, a loading/unloading time of 1 s, and a stress ratio (ratio of minimum to maximum load) equal to zero [6,19]. Crack growth in samples MS2 and MS3 is monitored through microradiographic images taken by interrupting the experiment every 15 cycles. The plot of the evolution of crack length with number of cycles is extrapolated backward to zero crack length to determine the exact number of cycles to crack initiation for all cracks in these samples. It is seen that the primary crack initiated at 83% life (550 cycles) for MS2 and at 85% life (380 cycles) for MS3. The results in Ref. [6] suggest that, generally, primary crack initiation in dwell fatigue occurs in the range 80–90% of total number of cycles to failure.

2.2 Finite Element Modeling of the Load Shedding Phenomenon. The performance of Ti alloys is often hindered by time dependent deformation characteristics at low temperatures, including room temperature [2,3,33,35]. This "cold" creep phenomenon occurs at temperatures lower than that at which diffusion-mediated deformation is expected (room temperature is about 15% of the homologous temperature for titanium). This creep process is of the transient kind or "exhaustion" type, i.e., the creep rate continually decreases with time. Consequently the creep process is not expected to be associated with diffusion-mediated mechanisms such as dislocation climb. Indeed, transmission electron microscopy (TEM) study has shown that deformation actually proceeds via dislocation glide, where the dislocations are inhomogeneously distributed into planar arrays. The planarity of slip has been attributed to the effect of short range order (SRO) of Ti and Al atoms on the hcp lattice [33]. Another common characteristic of cold creep in various Ti alloys with significant alphaphase content is that steady state is typically not achieved. This deformation mode is often referred to as "Andrade creep" due to the early documentation of such transients by Andrade for a number of metallic materials. In addition, significant creep strains can accumulate at applied stresses significantly smaller than the yield strength. Creep has been reported to occur at stresses as low as 60% of yield strength [35]. This characteristic has previously been attributed to rate sensitivity effects [2].

2.2.1 The Crystal Plasticity Based Constitutive Model. The α/β forged Ti-6242 is a biphasic polycrystalline alloy, which consists of colonies of transformed β phase in a matrix of the primary α phase. The primary α phase consists of equiaxed grains with a hcp structure, whereas the transformed β colonies have alternating α (hcp) and β (bcc) laths. The alloy considered in this study

Table 1 Material flow and hardness parameters for hcp Ti-6242 slip systems in tension

	a_1 basal	a_2 basal	a_3 basal	a_1 prism	a_2 prism	a_3 prism
$g_0{}^{\alpha}$ (primary α)	357.6	357.6	357.6	355.8	355.8	355.8
$g_0{}^{\alpha}$ (transformed β hcp)	349.9	382.0	382.0	305.9	255.8	287.4
m	0.02	0.02	0.02	0.02	0.02	0.02
$\dot{\bar{\gamma}}$ (s^{-1})	0.0023	0.0023	0.0023	0.0023	0.0023	0.0023

consists of 70% primary α and 30% transformed β grains. To incorporate the effect of various microstructural parameters, a size and time dependent large strain crystal plasticity based FE model has been developed in Refs. [3,7–9,20]. A homogenized model of the $\alpha+\beta$ phase colony regions in the Ti-6242 microstructure has been developed in Ref. [7]. The plastic part of the crystal plasticity equations involves a combined effect of slip on multiple slip systems. The plastic slip rate $\dot{\gamma}^{\alpha}$ on the αth slip system has a power law dependence on the resolved shear stress (τ^{α}) and the slip system deformation resistance (g^{α}), which evolve as

$$\dot{\gamma}^{\alpha} = \dot{\bar{\gamma}} \left| \frac{\tau^{\alpha} - \chi^{\alpha}}{g^{\alpha}} \right|^{1/m} \mathrm{sgn}(\tau^{\alpha} - \chi^{\alpha})$$
$$\dot{g}^{\alpha} = \sum_{\beta=1}^{\mathrm{nslip}} h^{\alpha\beta} |\dot{\gamma}^{\beta}| = \sum_{\beta} q^{\alpha\beta} h^{\beta} |\dot{\gamma}^{\beta}| \tag{1}$$

Here m is the material rate sensitivity parameter, χ^{α} is the back-stress that accounts for kinematic hardening in cyclic deformation, $h^{\alpha\beta}$ is the strain hardening rate due to self and latent hardening, h^{β} is self-hardening rate, and $q^{\alpha\beta}$ is a matrix describing the latent hardening. To account for size effects in polycrystalline materials, a Hall–Petch type relation for initial deformation resistance $g_0{}^{\alpha}$ with various characteristic length scales, depending on the slip direction, is incorporated into the model [9,20]. Material properties for each of the constituent phases and individual slip systems in the crystal plasticity model are calibrated in Ref. [7] with single colony and single crystal experiments. Calibrated values of important material constants are listed in Tables 1 and 2. Details of the microstructural morphology are accounted for in the model, through accurate phase volume fractions and orientation distributions that are statistically equivalent to those observed in orientation imaging microscopy (OIM) scans. The computational model is validated by comparing the results of simulations and constant strain rate and creep tests [7–9,20].

2.2.2 Image Based Statistical Representation of Actual Microstructures. The importance of representing critical morphological and crystallographic features of the microstructures in the accurate predictions of stress and strain localization and crack initiation has been emphasized in Refs. [10–12,20]. In the recent years, there have been significant advances in reconstruction and simulation of 3D polycrystalline microstructures based on information obtained from a dual beam focused ion beam-scanning electron microscope (FIB-SEM) system. This system is able to acquire 3D orientation or EBSD data from a series of material cross sections. This information has been successfully used in Ref. [10] for automatic segmentation of individual grains from the image and subsequently translated into a 3D mesh for finite element analysis (FEA). Through a multitude of data sets the intrinsic distributions of microstructural parameters can be captured and accurately represented through 3D microstructure reconstruction. Computational tools have been developed in Refs. [11,12] to create synthetic microstructures that are statistically equivalent to the measured structure with respect to certain microstructural features. These are used here for computationally efficient simulations to aid in the development of a microstructural crack initiation model. Microstructures are created from observations of two specific sites in the material samples, viz. (i) a critical region, in the vicinity of a dwell fatigue failure, and (ii) a noncritical region, away from it. The first sample considered is MS1. Two orientation imaging microscopy scans are performed on this sample; the first on a small critical region surrounding the primary crack tip, as

Table 2 Hardness parameters for hcp Ti-6242 slip systems in compression (m and $\dot{\bar{\gamma}}$ are the same as those in tension)

Primary α	a_1 basal	a_2 basal	a_3 basal	a_1 prism	a_2 prism	a_3 prism
$g_0{}^{\alpha}$ (primary α)	395.6	395.6	395.6	393.6	393.6	393.6
$g_0{}^{\alpha}$ (transformed β hcp)	450.9	574.7	590.6	448.5	571.1	586.9

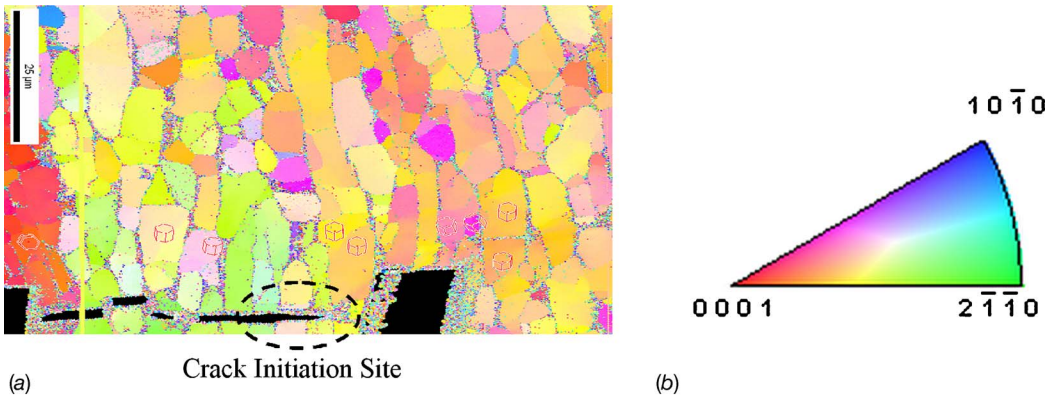

Fig. 2 (*a*) OIM scan of the critical primary crack initiation site in the MS1 microstructure and (*b*) scale

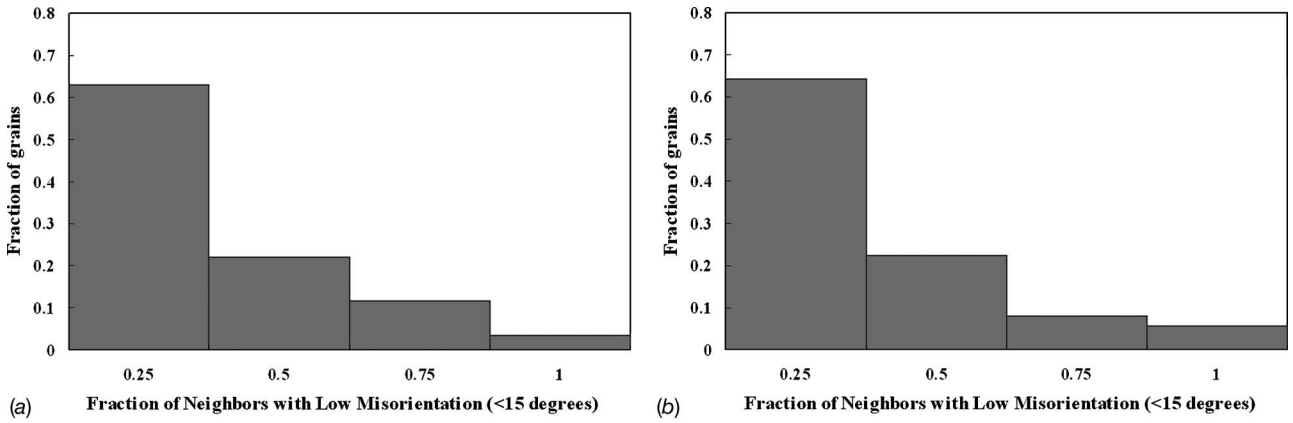

Fig. 3 Microtexture distributions (*a*) from OIM scan of critical region and (*b*) in the critical FE model of MS1

shown in Fig. 2, while the second on a noncritical region away from the crack. Two FE models of statistically equivalent simulated microstructures at the critical and noncritical regions are developed for analysis. In the development of the crack initiation model, it is expected that the initiation criterion will be met at some location in the critical FE model, but will not be satisfied in the noncritical FE model.

The following steps are performed for the construction of 3D microstructures from 2D OIM scans at the critical and noncritical sites. As discussed in Refs. [11,12], statistical distribution functions of various microstructural parameters in the 2D OIM scan are generated and subsequently projected in the third dimension for creating the 3D statistics. The assumptions and process implemented to extract 3D statistics from the 2D distributions of morphological and crystallographic features are briefly outlined as follows.

(i) *Distribution functions of grain size and shape*. An assumption made here is that grain sections in the 2D OIM scans have a similar size and shape correlation to their parent 3D structures, as elliptical sections through ellipsoidal 3D grains have to each other. For determining the size and shape distributions of the 3D grains in the microstructure, a large number of ellipsoids of various sizes and shapes are randomly sectioned and the resulting elliptical sections are recorded. Probabilistic weighting functions are created for the grain reconstruction process. The 3D ellipsoid that produces an elliptical section closest in shape and size to a 2D OIM grain scan is assumed to have a high probability in the representing corresponding 3D grain. An assumption is needed for the orientation distribution of the ellipsoids relative to the sectioning plane of the OIM scan. While in Ref. [12], three orthogonal sections have been taken, in the present work, only one section of the surface scan is available, and the orientation distribution is assumed to be random. A constrained Voronoi tessellation, with initial seed points at the centroid of the ellipsoid, is executed for generating the grain shapes.

(ii) *Distribution of number of neighbors*. The reconstructed 3D grains are placed in a representative cubic volume with a constraint that each grain has appropriate number of neighbors, as determined by 3D projection of the OIM scan. In the 2D OIM scan, each grain has approximately 3–12 neighbors, while grains in the 3D representation have 8–25 neighbors. The representative cube of dimensions $65 \times 65 \times 65$ μm^3 for the MS1 microstructure consists of 949 grains.

(iii) *Distribution of crystallographic orientations*. The crystallographic orientation assignment to the grains in the cubic volume is executed by the three major steps described in Refs. [7,11]. These are delineated as (a) orientation probability assignment method (OPAM), (b) misorientation probability assignment method (MPAM), and (c) microtexture probability assignment method (MTPAM). Figure 3 shows the microtexture distribution in the 2D scan and in the 3D model, with satisfactory agreement.

The reconstructed 3D model has distributions of orientation, misorientation, microtexture, grain size, and number of neighbors that are statistically equivalent to those observed experimentally from the OIM scan. The model is subsequently discretized into a finite element mesh of 78,540 tetrahedron elements, as shown in Fig. 4.

2.2.3 Mesh Convergence Study. Since local variables in the finite element simulations are pivotal to the development of the nucleation criterion, a sensitivity study of the local variables with respect to mesh density is done prior to the dwell fatigue analysis. The MS1 microstructure is used for this study with two different mesh densities. Both FE models have the same number of grains, i.e., 949 and the same orientation, misorientation, microtexture, and grain size distributions. The first model consists of 78,540 elements, while the second has 116,040 elements, which is approximately 150% higher in mesh density. A creep simulation is performed for both these models for 1000 s at an applied load of

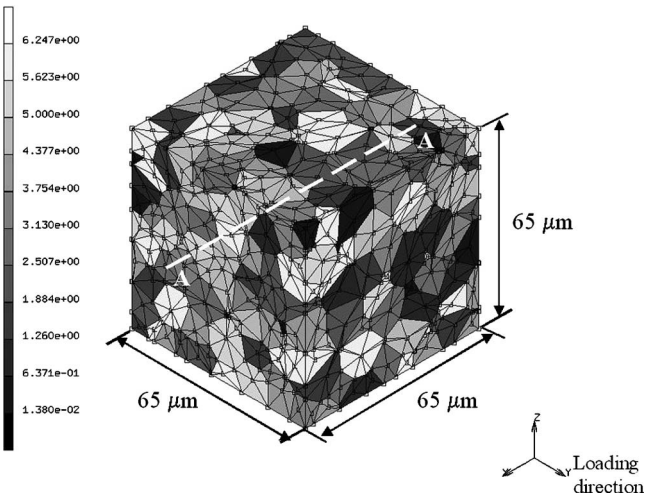

Fig. 4 FE model for polycrystalline Ti-6242, which is statistically equivalent to the OIM scan of the critical region of microstructure MS1. Also shown is the contour of the *c* axis orientation distribution (radians).

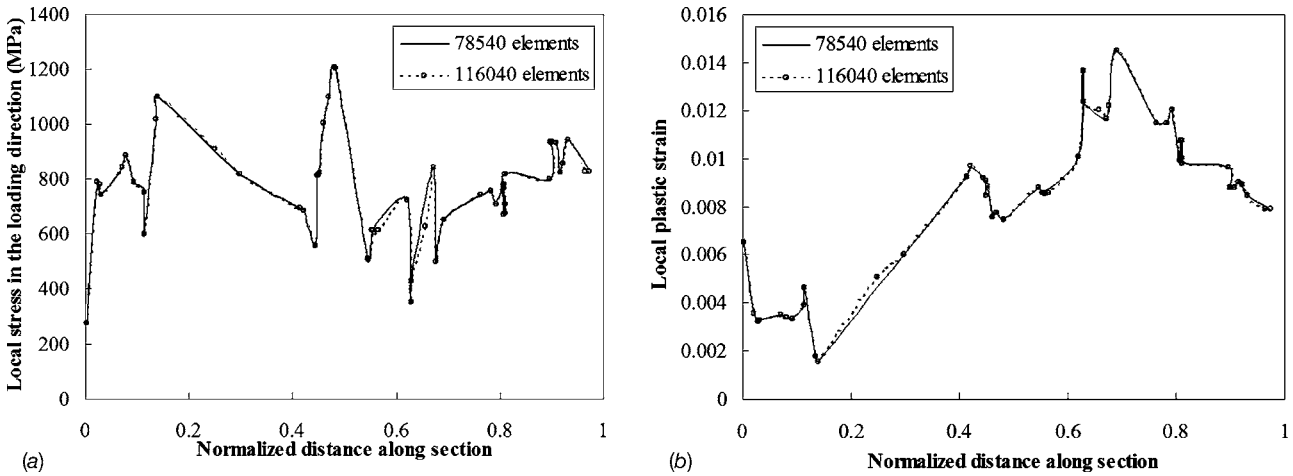

Fig. 5 Distribution of local variables: (*a*) loading direction stress (σ_{22}) and (*b*) local plastic strain along a section parallel to the *x*-axis at the end of 1000 s for a creep simulation on the two models of microstructure MS1 with two different mesh densities

869 MPa in the *Y*-direction. The local stress component in the loading direction and the local plastic strain at the end of 1000 s are compared for various sections in the FE models. The stresses are found to be in good agreement for the two models. Plots comparing the distribution of these variables along a section parallel to the *X*-axis in Figs. 5(*a*) and 5(*b*), show excellent agreement between the two models. These results indicate that the 78,540 element mesh is a converged mesh for the loading considered, and is henceforth used in this study for the development of the crack initiation criterion.

2.2.4 Load Shedding Simulation in Polycrystalline Ti-6242. A dwell fatigue simulation is performed for the microstructure MS1 to understand the effect of microstructure on the load shedding behavior. The simulation is run for 352 cycles, i.e., the life of the sample [6] with loading conditions mentioned in Sec. 2.1.2. The time dependent tensile dwell loading is applied on the $Y = 65$ μm face in the *Y*-direction. Figure 6(*a*) plots the local stress σ_{22} after 1 cycle and 300 cycles, respectively, along a section A-A shown in Fig. 4. Section AA passes through a hard-soft grain combination, from the prominent Schmid factor plot in Fig. 6(*b*) that corresponds to the prismatic slip system. Figure 6(*a*) shows a stress peak at point *X*, while a valley at point *Y*. The stress peak at *X* at 300 cycles is considerably higher than that at 1 cycle, and much higher than the applied stress. The peak stress increases with time, while the valley drops with time due to load shedding caused by plastic strain at point *Y*. From Fig. 6(*b*) it is seen that the point *X* has a low SF (~0.11), while *Y* has a high SF (~0.49). This high mismatch in SF causes load shedding from grain at point *Y* onto the grain at point *X*. These observations are consistent with the results of simulations in Refs. [7–9,21]. This analysis demonstrates the importance of load shedding induced stress concentrations in a hard grain on the development of a microstructure level criterion for crack initiation.

3 Crack Nucleation Criterion Accounting for Dislocation Pileup

Crack nucleation phenomena have been considered at different length scales in literature [21]. In this section, a crack nucleation criterion is proposed at the length scale of individual grains in terms of slip system variables obtained from crystal plasticity FE solution. High stresses at the tip of dislocation pileups, which build at grain boundary barriers, are often responsible for microcrack nucleation. Stress concentration induced crack nucleation at the grain boundary of a crystalline solid has been explained in Ref. [13] using a dislocation pileup model. Considering only Mode I crack, the model proposes that a crack is initiated if $n\sigma_n \geq 12\alpha G$, where n is the number of dislocations in the pileup, σ_n is

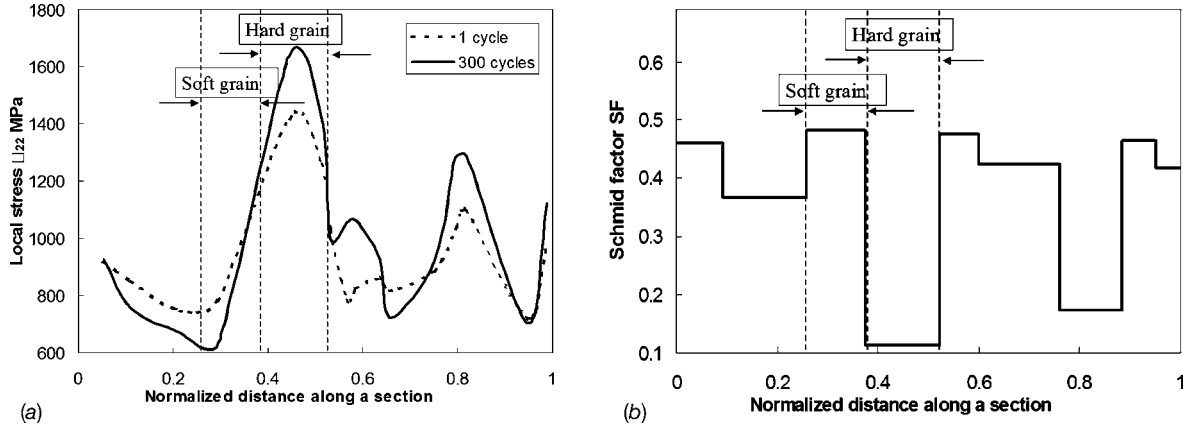

Fig. 6 Distribution of local variables: (*a*) loading direction stress (σ_{22}) and (*b*) prominent prismatic Schmid factor along a section AA parallel to the *x*-axis at the end of 1 dwell cycle and 300 dwell cycles for a dwell fatigue simulation of the MS1 model

the stress normal to the slip plane, G is the shear modulus, and $\alpha = \gamma/\boldsymbol{b}G$ is a material constant, in which γ is the surface energy and $\boldsymbol{b}$ is the Burgers vector. However, Bache [4] argued about a combined effect of normal and shear stresses, responsible for dwell fatigue of Ti alloys. Various dislocation level fatigue failure models [13,14,22–24] have discussed equivalence in the dependencies of crack evolution ahead of dislocation pileups and at crack tips, and have demonstrated the equivalence between continuous dislocation pileups and cracks. This equivalence in the functional forms is exploited in this work to develop a grain-level crack nucleation criterion.

The proposed framework for microcrack nucleation builds on the fracture criterion proposed in Ref. [25], where catastrophic fracture occurs when strain energy release rate is sufficient to overcome the rate of surface energy needed for breaking of bonds, as well as energy dissipation due to plastic flow, stated as

$$\sqrt{\sigma^2 + \beta\tau^2} \geq \alpha_1 \sqrt{\frac{\mathcal{G}_c}{a_0}} \tag{2}$$

Here σ is the normal stress, τ is the shear stress acting on the plane of the crack, and β is a shear stress factor, which is used to assign different weights to the normal and shear traction components for mixed mode, defined as the ratio of the shear to normal fracture toughness of the material, i.e., $\beta \approx K_{\mathrm{IIC}}/K_{\mathrm{IC}}$ in Ref. [26]. a_0 is the pre-existing crack length, $\mathcal{G}_c$ is the critical strain energy release rate, and α_1 is a material dependent parameter. A similar criterion is also derived from a stress intensity approach [27], where the material is assumed to withstand crack tip stresses up to a critical value of the stress intensity factor K_{Ic}, stated as

$$\sqrt{\sigma^2 + \beta\tau^2} \geq \alpha_2 \frac{K_{Ic}}{\sqrt{a_0}} \tag{3}$$

Here, α_2 is a geometry dependent parameter. In a similar vein, a brittle crack initiation criterion is postulated in this work due to stress concentration in the hard grain caused by dislocation pileup in the neighboring soft grains. Microcracking is triggered when the effective stress in a slip system, represented in terms of slip system normal and tangential stress components, reaches a critical value. The stress component normal to a given slip plane is expressed as $T_n = n_i^b(\boldsymbol{\sigma}_{ij} n_j^b)$, where $\boldsymbol{\sigma}_{ij}$ is the Cauchy stress tensor and n_i^b corresponds to components of the unit outward normal to the slip plane. Only the tensile normal stress $\langle T_n \rangle$, represented by the McCauley bracket $\langle\ \rangle$, is considered since compressive stresses will not contribute to opening a crack. The shear stress component T_t is obtained by the vector subtraction of $\boldsymbol{T}_n$ from the stress vector on the plane, i.e., $T_t \boldsymbol{t}^b = \boldsymbol{T} - \boldsymbol{T}_n \boldsymbol{n}^b$, where $\boldsymbol{t}^b$ is the unit vector tangent to the plane. The effective resultant traction T_{eff} is defined as $T_{\mathrm{eff}} = \sqrt{\langle T_n \rangle^2 + \beta T_t^2}$.

Continuous dislocation pileups at a barrier, e.g., at the boundary of a soft grain adjacent to a hard grain, have been shown to be equivalent to cracks, e.g., in Ref. [14], in the way they cause stress concentration at their tip. The dislocation pileup acts in a similar way as a crack, whose length scales with the length of the pileup. Correspondingly, the right-hand side (RHS) of Eq. (2) may be amended with an inverse square root dependence on the pileup length d. The resulting microcrack nucleation criterion may be stated as

$$T_{\mathrm{eff}} = \sqrt{\langle T_n \rangle^2 + \beta T_t^2} \geq \frac{R_c}{\sqrt{d}} \tag{4a}$$

or, equivalently,

$$R = T_{\mathrm{eff}} \cdot \sqrt{d} \geq R_c(b) \tag{4b}$$

where R_c is a parameter that depends on the material elastic properties, as well as on the critical strain energy release rate $\mathcal{G}_c$. It has the units of stress intensity factor (MPa $\sqrt{\mu\mathrm{m}}$). A value of $\beta = 0.7071$ that has been suggested for Ti-64 alloys in Ref. [28] is used in this study. Sensitivity analysis with different values of β indicate that T_{eff} is not very sensitive to β for $\langle c+a \rangle$ oriented hard grains, since $T_n \gg T_t$. As more dislocations are added to the pileup with time, the pileup length d in the soft grain increases. This implies a smaller T_{eff} to initiate a crack with increasing plastic deformation and pileup.

3.1 Estimating the Dislocation Pileup Length *d*. The crystal plasticity FEM model developed in Refs. [7–9] does not explicitly have dislocations densities as a state variable. Hence an inverse relation is used to estimate the dislocation pileup length d from the plastic strains and its gradients that are available from the results of the crystal plasticity FE simulations. This provides the nonlocality aspect of the crack nucleation criterion. To begin with, a continuous dislocation density distribution function per unit length $\rho^l(x)$ has been derived in Ref. [29] as a function of the distance x from the dislocation barrier and pileup length d as

$$\rho^l(x) = \frac{2\tau}{G\boldsymbol{b}} \sqrt{\frac{d-x}{x}}, \quad \Rightarrow \quad d = \left(\frac{[\rho^l(x)]^2 G^2 \boldsymbol{b}^2}{4\tau^2} + 1 \right) x \tag{5}$$

where G is the shear modulus, τ is the shear stress, and $\boldsymbol{b}$ is the magnitude of the Burgers vector. The dislocation density per unit length $\rho^l(x)$ may be obtained by multiplying the dislocation density per unit area $\rho^A(x)$ with the dislocation line length. The total dislocation density $\rho^A(x)$ is assumed to be the sum of the density of statistically stored dislocations (SSDs) corresponding to homogenous plastic deformation and the density of geometrically necessary dislocations (GNDs) that accommodate plastic strain gradients, which may be expressed as (see Ref. [30])

$$\rho^A{}_{\mathrm{SSD}} = \frac{\sqrt{3}\bar{\varepsilon}^P}{b l^*} \quad \text{and} \quad \rho^A{}_{\mathrm{GND}} = \frac{\eta^P}{b} \tag{6}$$

where l^* denotes the material length scale, which is of the order of $(G/\sigma_{\mathrm{yield}})^2 \boldsymbol{b}$, as discussed in [31]. In Ref. [32], its value is given as $l^* = 3\alpha^2 (G/\sigma_{\mathrm{yield}})^2 \boldsymbol{b}$, where α is an empirical constant. In the present work, l^* is taken to be the average grain size, which is $\sim 5\ \mu$m from Ref. [32]. The equivalent plastic strain and a measure of the effective plastic strain gradient are defined in terms of the plastic part of the deformation gradient tensor $\boldsymbol{F}^P$, which is available from the FEM output data, as

$$\begin{aligned} \bar{\varepsilon}^p &= \det\left(\frac{2}{3} \left\{ \frac{1}{2}(\boldsymbol{F}^{p^T}\boldsymbol{F}^p - \mathbf{I}) \right\}^T \left\{ \frac{1}{2}(\boldsymbol{F}^{p^T}\boldsymbol{F}^p - \mathbf{I}) \right\} \right)^{1/2} \\ \eta^p &= \left(\frac{1}{\det \boldsymbol{F}^P} \boldsymbol{F}^P \,.\, (\boldsymbol{\nabla} \times \boldsymbol{F}^P) : \frac{1}{\det \boldsymbol{F}^P} \boldsymbol{F}^P \,.\, (\boldsymbol{\nabla} \times \boldsymbol{F}^P) \right)^{1/2} \end{aligned} \tag{7}$$

The curl of the plastic deformation gradient, expressed as $\boldsymbol{\nabla} \times \boldsymbol{F}^p = \varepsilon_{irs}(\partial F^p{}_{js}/\partial x_r)$ with ε_{irs} being the permutation symbol, is a third order tensor with 27 components. Numerically, each component of $\partial F_{ij}^p/\partial x_r$ may be calculated using a weighted difference formula involving surrounding points as

$$\frac{\partial F_{ij}^p}{\partial x_r} = \frac{\displaystyle\sum_{m=1}^{n} \frac{1}{r_m} \left(\frac{(F_{ij}^p)_k - (F_{ij}^p)_m}{(x_r)_k - (x_r)_m} \right)}{\displaystyle\sum_{m=1}^{n} \frac{1}{r_m}} \tag{8}$$

where n is the number of points that lie within a sphere of assumed radius ($\sim 5\ \mu$m) from the kth point at which $\partial F_{ij}^p/\partial x_r$ is being evaluated within the grain. The weighting function is taken as the inverse of r_m, which is the distance between the kth point and the surrounding mth point. Since $\boldsymbol{F}^P$ is a state variable in the crystal plasticity FE simulations, $\bar{\varepsilon}^P$ and η^P in Eq. (6) can be determined at integration points using the expressions given

above. Once, the two components are evaluated from Eq. (6), the total dislocation density per unit area $\rho^A(x)$ can be determined using

$$\rho^A(x) = \rho^A{}_{\mathrm{SSD}}(x) + \rho^A{}_{\mathrm{GND}}(x) \tag{9}$$

The dislocation density $\rho^l(x)$ in Eq. (5) is subsequently obtained from $\rho^A(x)$. For $\langle a \rangle$ type slip in Ti-6242, the dislocation line length has been determined to be ~ 250 nm in Ref. [33]. Since the dislocation density may be the result of slip on multiple planes, no one plane is chosen for calculating x toward evaluating the pileup length d in Eq. (8). In consistency with the effective dislocation density measure, x is taken as the distance of the integration point to the nearest grain boundary. The pileup length d in Eq. (5) is restated as

$$d = [(A_1\varepsilon^p + A_2\eta^p)^2 + 1]x \quad \text{where} \quad A_1 = \frac{\sqrt{3}G}{2\pi l^*}, \quad A_2 = \frac{G}{2\tau} \tag{10}$$

It may be emphasized that the parameters in the above equations are calibrated from experiments and crystal plasticity simulations and hence the explicit forms of the parameters are not required for calculations.

In the FE model, each grain is meshed with several elements and hence each grain boundary is shared by a number of elements. Thus, an effective dislocation pileup length $\bar{d}$ for a given grain boundary is computed as the weighted average of pileup lengths d_i corresponding to multiple integration points in the soft grain adjacent to a hard grain, i.e.,

$$\bar{d} = \frac{\sum_{i=1}^{p} W(r_i) d_i}{\sum_{i=1}^{p} W(r_i)} \tag{11}$$

where p is the number of integration points in consideration, r_i is the distance between the point at which the criterion is being evaluated and the element integration point i in the soft grain and the weighting function is given in Ref. [34] as $W(r) = (1/(2\pi)^{3/2} l^3)\exp(-r^2/2l^2)$. This weighting function tends to zero beyond a certain distance. The parameter l determines the size of the region that contributes to $\bar{d}$. Numerical sensitivity analysis on the effect of l on the value of R at different locations infers that R does not vary much for $l \geq 5$ μm. Finally, substituting Eqs. (10) and (11) into Eq. (4) yields the grain-level crack nucleation criterion as

$$T_{\mathrm{eff}} = \sqrt{\langle T_n \rangle^2 + \beta T_t^2} \geq \frac{R_c}{\sqrt{\dfrac{\sum_{i=1}^{p} W(r_i)[(A_1\varepsilon_i^p + A_2\eta_i^p)^2 + 1]x_i}{\sum_{i=1}^{p} W(r_i)}}} \tag{12a}$$

or equivalently

$$R = T_{\mathrm{eff}} \cdot \sqrt{\frac{\sum_{i=1}^{p} W(r_i)[(A_1\varepsilon_i^p + A_2\eta_i^p)^2 + 1]x_i}{\sum_{i=1}^{p} W(r_i)}} \geq R_c \tag{12b}$$

The left-hand side of Eq. (12*a*) evaluates T_{eff} at a point in a (hard) grain, while the right hand side incorporates the plastic strain ε^P and its gradient η^P in an adjacent softer grain. The variable R is checked for every element integration point near the grain boundary in the crystal plasticity FE model in the postprocessing stage. Various parameters used in Eq. (12) are listed in Table 3. The condition posed in Eq. (12) is nonlocal in that the stress required to initiate a crack at a point in the hard grain depends on the plastic strain and gradient of plastic strain in the neighboring soft grain.

Table 3 Parameters used in the crack nucleation criterion of Eq. (12)

Material parameter	Value
Shear modulus, G	48 GPa
Magnitude of Burgers vector, $\boldsymbol{b}$	0.30 nm
Material length scale, l^*	5 μm
Nonlocal length parameter, l	5 μm

There is some nonuniqueness in the estimation of the length of dislocation pileup at the grain boundary. One can get an estimate of the dislocation pileup length in this context by other methods. In the present formulation, Eq. (5) is a direct analytical expression for the dislocation pileup length in terms of the density function per unit length based on a single slip system activity. Since this formulation does not directly yield $\rho^l(x)$, this formulation tries to connect this to the total dislocation density per unit area $\rho^A(x)$ based on a multislip system. To establish this connection, the dislocation pileup for $\rho^A(x)$ is assumed to follow the same distribution function as that for single slip $\rho^l(x)$ in Eq. (5). The dislocation density per unit length is obtained by multiplying the dislocation density per unit area by a dislocation line width, with the implicit assumption that the variation in $\rho^l(x)$ in the direction perpendicular to the distance from the grain boundary is negligible.

4 Calibration and Validations of the Nucleation Criterion

4.1 Calibration of R_c for α/β Forged Ti-6242. The material parameter R_c in the RHS of Eq. (12*a*) is calibrated from the results of the 2 min dwell fatigue FE simulations of the microstructure MS1 for 352 cycles. Based on the observations made for the samples MS2 and MS3 in Sec. 2.1.2, initiation is assumed at two alternate percentages of the total life, viz. 80% and 85% (i.e., 282 cycles and 300 cycles). To calibrate R_c corresponding to the two percentages, the variable R in Eq. (12*b*) is determined at integration points closest to each grain boundary for all grains at the end of 282 cycles and 300 cycles. The hard grain of the grain pair with a maximum value of R is located in Fig. 4 and the evolution of this maximum R with number of cycles is plotted in Fig. 7(*a*). From Eq. (12*b*), assuming initiation to have occurred at these fractions, the value of R may be equated to R_c. For the two scenarios, the threshold values are determined to be $R_{c(80\%)} = 454.44$ MPa$(\mu\mathrm{m})^{1/2}$ and $R_{c(85\%)} = 459.38$ MPa$(\mu\mathrm{m})^{1/2}$. These parameters are used for predicting crack initiation in other experiments and studies.

4.2 Predictions and Analysis With Samples MS2 and MS3. For the MS2 microstructure, the FE model is generated to be statistically equivalent to an OIM scan surrounding one of the secondary cracks in the failed sample. The crack initiation for that crack is determined to occur at 530 cycles from Ref. [6], as described in Sec. 2.1.2. The 2 min dwell fatigue FE simulation is performed for 663 cycles with loading conditions described in Ref. [6]. Figure 7(*b*) shows the evolution of the maximum R with cycles. The number of cycles to initiation $N_{c(80\%)}$ and $N_{c(85\%)}$ are predicted for MS2 from where the evolution curve meets the calibrated threshold values $R_{c(80\%)}$ and $R_{c(85\%)}$. The corresponding cycles to initiation are found to be $N_{c(80\%)} = 502$ and $N_{c(85\%)}$

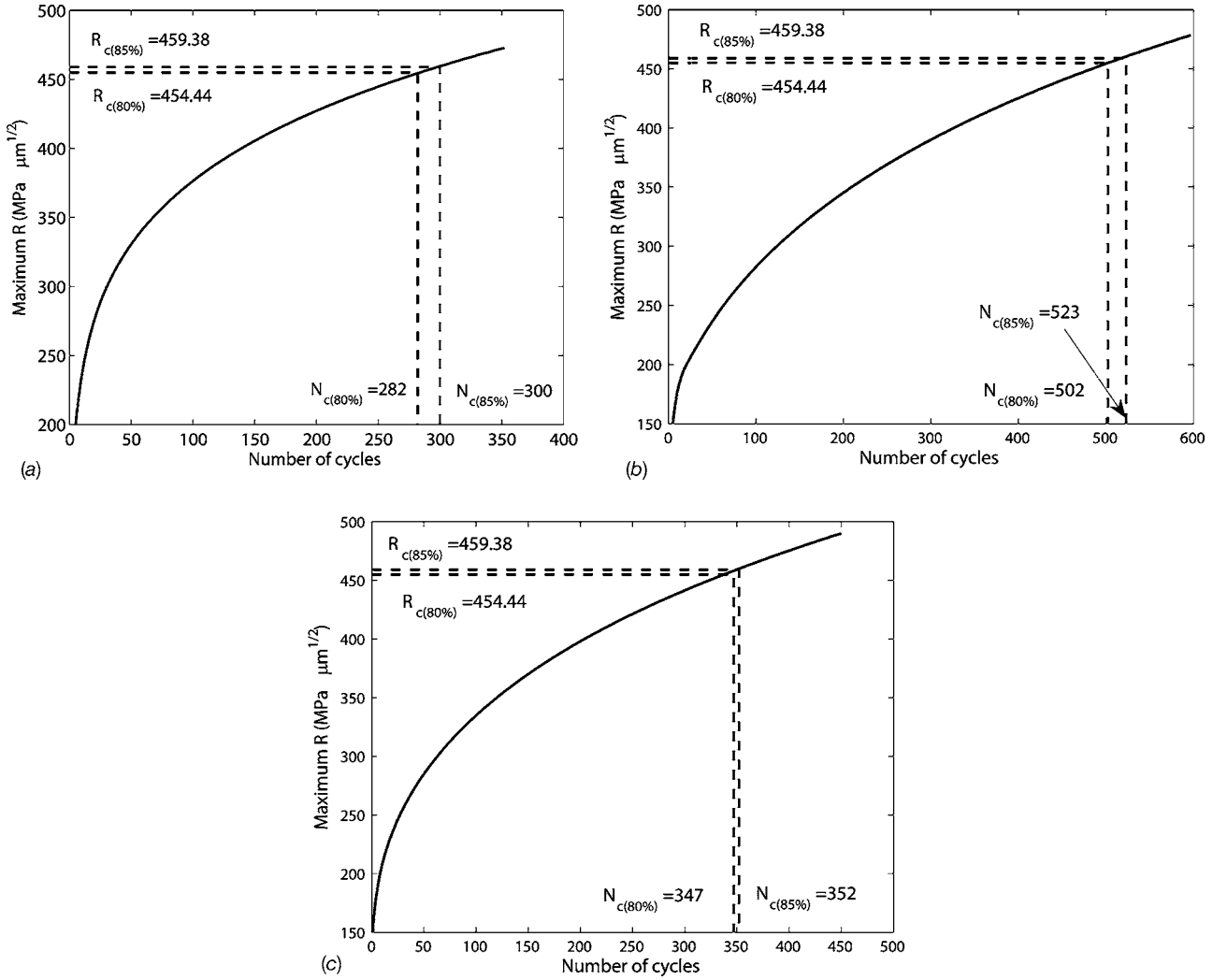

Fig. 7 Evolution of the maximum *R* over number of cycles for the FE models of microstructures (*a*) MS1, (*b*) MS2, and (*c*) MS3

=523. The difference in the experimentally determined value of 530 cycles is 5.28% for 80% of life and only 1.32% for 85% of life. This agreement is considered to be excellent.

Likewise, for the MS3 microstructure, the FE model is generated using statistics of corresponding critical regions at the failure site, and the 2 min dwell fatigue simulation is performed for 447 cycles. The evolution of the maximum R is plotted in Fig. 7(c). The cycles to initiation for MS3 are predicted to be $N_{c(80\%)}$ =347 and $N_{c(85\%)}$=352. The differences with the experimentally determined values are 8.68% for 80% of life and 7.37% for 85% of life. The results are summarized in the Table 4. In general, the calibrated value of R_c at 85% life is seen to work better than at 80% life. As an additional validation study, the predicted locations of crack initiation in these microstructures are examined and summarized in Table 5. It can be seen that in each case, crack initiation is predicted for a grain with low c axis orientation (~0–30 deg), low prism SF (~0–0.1), and low to moderate basal SF (~0.3–0.45), which is consistent with the observations in Ref. [18]. These results prove convincingly the predictive capability of the proposed criterion. The model is expected to be extrapolated to other materials, as long as the same mechanisms for dwell fatigue hold. Currently, a more diverse set of loading conditions are being tested for the versatility of this model.

5 Sensitivity Studies of Nucleation Criterion to Critical Microstructural Parameters

In this section, the sensitivity of the crack nucleation criterion is examined for a few critical microstructural conditions that have been observed to significantly affect load shedding behavior and the dwell fatigue life of Ti-6242 in Refs. [5,20].

Table 4 Comparison of predicted cycles to crack initiation with experimentally observed life

		Time to crack initiation (predicted)		% relative error	
Microstructure label	Time to crack initiation (experiment) (cycles)	Calibrated at 80% life (cycles)	Calibrated at 85% life (cycles)	Calibrated at 80% life	Calibrated at 85% life
MS2	530	502	523	5.28	1.32
MS3	380	347	352	8.68	7.37

Table 5 Microstructural features of predicted location of crack initiation in dwell fatigue of Ti-6242

Microstructure label	θ_c (deg)	SF prism	SF basal
MS1	29.39	0.1134	0.426
MS2	17.86	0.0047	0.2832
MS3	32.05	0.133	0.447

5.1 Schmid Factor Mismatch Between Grains. Sensitivity of the crack nucleation criterion to the Schmid factor mismatch between hard and soft grains is studied through dwell fatigue simulations on a FE model of a two-grain system. The system consists of an inner hard grain contained in an outer soft grain. The mesh is highly refined at the grain boundary to enable capture of the high stress and strain gradients. The hard grain has all the basal and prismatic SFs nearly equal to zero, while the orientation of the soft grain is chosen so that a desired SF on the a_1 basal slip system is achieved. Four cases, with different a_1 basal SF of the soft grain, viz. 0.425, 0.45, 0.475, and 0.5, are considered. In each case, the sizes of the hard and soft grains are fixed at 5 μm and 50 μm, respectively. A 2 min dwell fatigue simulation is carried out for each case with a maximum load of 535 MPa, which corresponds to 95% of the lowest yield stress of the four cases. The dwell cycle, in which the condition $R=R_{c(85\%)}$ is satisfied, is taken as the number of cycles to crack initiation for that case. The calibrated value of $R_{c(85\%)}$ for α/β Ti-6242 from Sec. 4.1 is used for this purpose. Figure 8(*a*) shows the predicted cycles to initiation as a function of the corresponding mismatch in a_1 basal SF of the grains. An increase in the mismatch by 0.025 affects the predictions by an order of magnitude. For example, when the mismatch is 0.5, the crack nucleation criterion predicts just ~100 cycles to initiation, while for a mismatch of 0.425, it predicts $\sim 1.81\times 10^5$ cycles. It is evident from these results that the predictions of the criterion are highly sensitive to the SF mismatch between grains.

5.2 Size of Soft Grain. Sensitivity of the predictions of the crack initiation criterion to the size of the soft grain is studied for the two-grain model. Four cases are considered with different soft grain sizes, viz. 5 μm, 25 μm, 50 μm, and 75 μm. In each case, the size of the hard grain is fixed at 5 μm and the a_1 basal SF of the soft grain at 0.5. The number of cycles to crack initiation in a 2 min dwell fatigue simulation for each case is predicted and plotted as a function of the size of the soft grain in Fig. 8(*b*). The criterion is sensitive to the size of the soft grain as well. For example, when the soft grain size is 50 μm, crack initiation is predicted at ~100 cycles, and when the soft grain size is 5 μm, crack initiation is predicted at $\sim 2\times 10^5$ cycles. It is interesting to note that in contrast to the trend of predictions for SF mismatch,

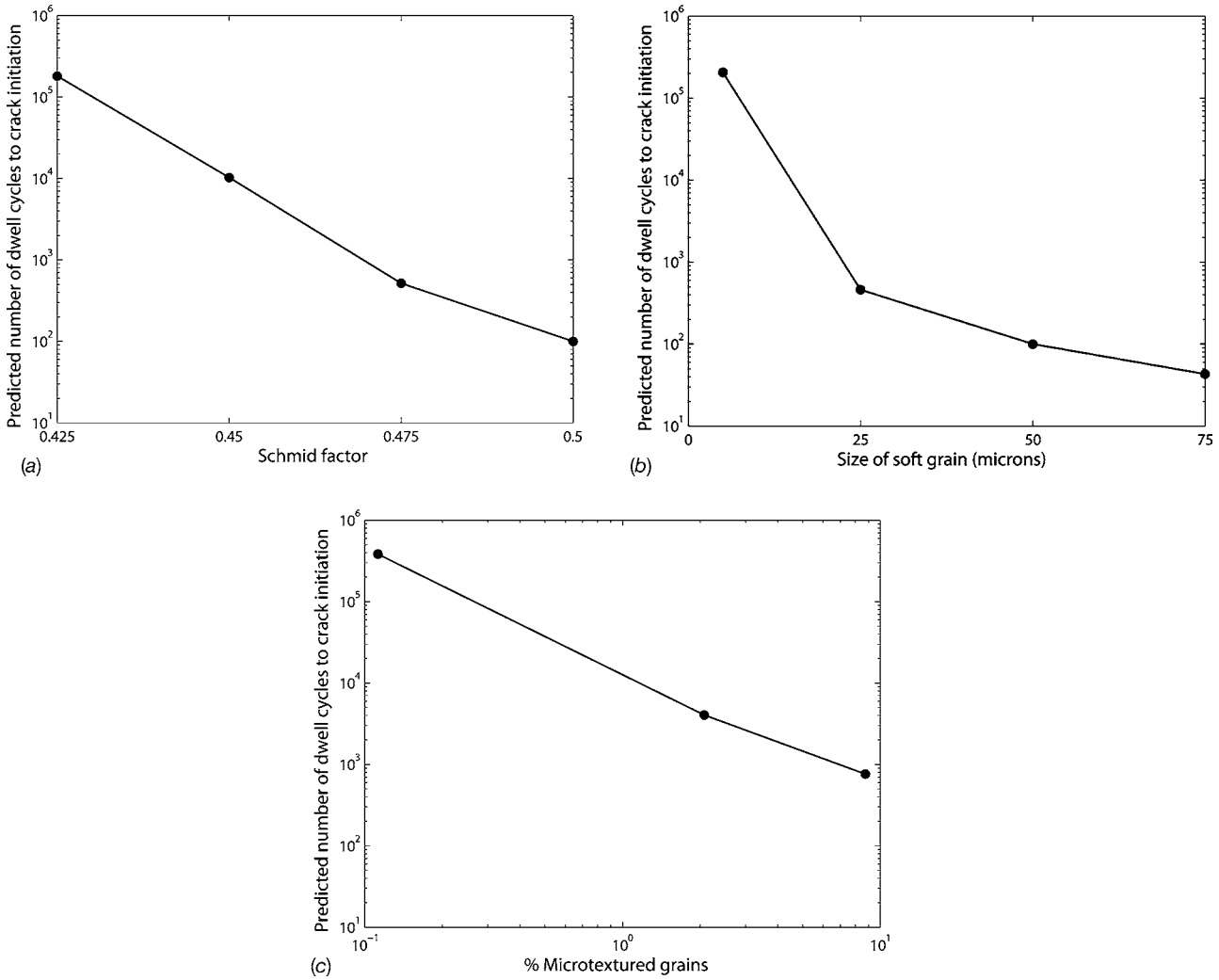

Fig. 8 Variation in predicted number of cycles to crack initiation by the criterion with (*a*) Schmid factor mismatch, (*b*) size of soft grain, and (*c*) level of microtexture

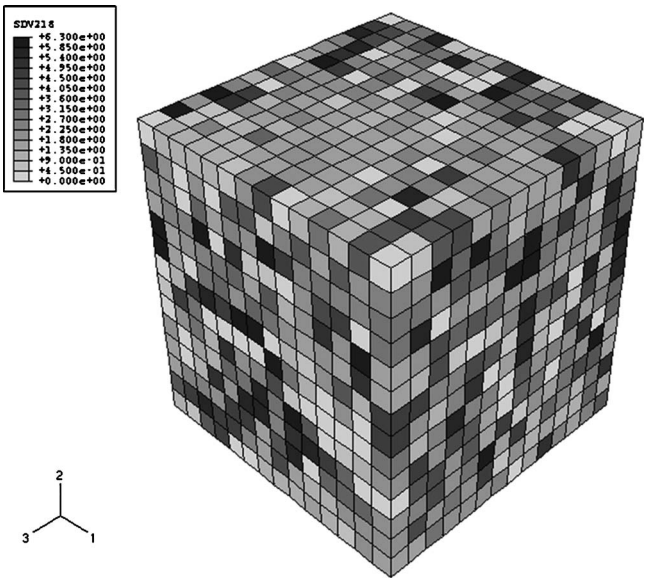

Fig. 9 FE model for polycrystalline Ti-6242, which is statistically equivalent to the OIM scan of α/β forged Ti-6242. Also shown is the contour of *c* axis orientation distribution (radians).

the decrease in the predicted number of cycles with increasing grain size decays in nature. The difference between the predictions for the sizes of 5 μm and 25 μm is much higher than the difference between the predictions for the sizes of 50 μm and 75 μm. This trend indicates that the criterion also senses the inverse square root relation between the initial slip system deformation resistance g^{α} and the grain size [9,20] and is able to predict the decaying influence of increasing grain size on load shedding.

5.3 Microtexture. Sensitivity of the criterion is now tested with respect to local texture in a polycrystalline microstructure. The study involves predictions of the crack nucleation criterion for different levels of microtexture. The FE model consists of a unit cubic domain discretized into 8000 trilinear brick elements. Each element in the FE representation of polycrystalline Ti-6242 aggregate shown in Fig. 9 represents a single grain. Three sets, each with 8000 grain orientations, but with different levels of microtexture, are generated and assigned to the polycrystalline model. The metric used for the level of microtexture is the percentage of grains that have a low misorientation (<15 deg) with a large fraction of their neighbors ($>66.66\%$). These percentages for the three cases are 0.1125% for low microtexture, 2.075% for intermediate microtexture, and 8.75% for high microtexture. For each case, a 2 min dwell fatigue simulation is run at an applied load of 800 MPa, which corresponds to 95% of the lowest yield point of the three models. The number of cycles to crack initiation is predicted when the condition $R=R_c$ is satisfied at any location. These predictions are plotted in Fig. 8(*c*). It is seen that for a high microtexture, the crack nucleation criterion predicts 761 cycles to crack initiation, while for the low microtexture or a random texture, it predicts $\sim 3.84\times 10^5$ cycles. These predictions are consistent with Ref. [5], where a similar order of magnitude difference in the dwell fatigue lives of Ti-6242 samples with high and low microtextures has been reported. This analysis demonstrates the microstructure sensitivity of the crack nucleation criterion.

6 Simulations of Dwell Fatigue Field Tests on β Forged Ti-6242

6.1 Mechanical Tests on β Forged Ti-6242. As a part of the dwell fatigue investigation of Ti-6242, a set of cyclic loading experiments has been performed at Honeywell [15] on β forged Ti-6242, which consists of only the transformed β phase. Two experiments from this set, viz. (i) normal fatigue test and (ii) 2 min dwell fatigue test, are considered in this work. Both experiments have been performed at a maximum load of 897 MPa and stress ratio of 0.1. The life of the normal fatigue sample has been recorded as 24,241 cycles, while that of the dwell fatigue sample as 20,141 cycles. The small difference in these two lifetimes shows that the alloy exhibits negligible dwell sensitivity.

6.2 Dual Time Scale Simulation Technique for Cyclic Deformation. It is computationally prohibitive to simulate large number of cycles, $\sim$20,000 cycles in this case, using the FE model of the polycrystalline microstructure with a single time scale simulation. An enormous number of time increments for the problem with a large number of degrees of freedom paralyze the simulation. Extrapolation techniques have been employed in literature with results from a limited number of cycles to predict variables at a large number of cycles. This however results in loss of accuracy, especially in the microstructural variables, due to the process of history dependent localization.

To enable accurate analysis for a large number of cycles, even at the microstructural scale, a multitime scaling method has been developed in Ref. [16]. This methodology involves decoupling of the governing equations into two sets of problems corresponding to two different time scales. When subjected to an oscillating load, the deformation behavior exhibits an oscillatory behavior about an averaged or "macroscopic" evolution of state variables. The frequency or rate of change of averaged variables is generally quite low in comparison with the frequency of the applied cyclic loads. Consequently, it is conceivable to introduce two different time scales in the solution, viz. (i) a coarse time scale t, for the average variables, which can be solved by time increments that are significantly longer than the period of a single cycle, and (ii) a fine time scale τ that is necessary for providing adequate resolution to the rapidly varying behavior due to the oscillating load.

The relation between the two time scales t and τ is defined as $t=\varepsilon\tau$, where $\varepsilon \ll 1$ is a small positive scaling parameter. A superscript ε associated with a variable denotes its association with both the time scales. Consequently, all the response fields in the body at a given spatial location x are assumed to exhibit dependence on the coarse time scale t and the fine time scale τ and is expressed as $\phi^{(\varepsilon)}(x,t)=\phi(x,t,\tau)$. Using the chain rule, and the relation between time scales, the time derivative in the two time scales is given as

$$\dot{\phi}^{(\varepsilon)} = \frac{\partial \phi^{(\varepsilon)}}{\partial t} = \frac{\partial \phi}{\partial t} + \frac{1}{\varepsilon}\frac{\partial \phi}{\partial \tau} \tag{13}$$

The cycle averaged field variable over a period T in the fine time scale $\tau=t/\varepsilon$, at time t is defined as,

$$\bar{\phi}(t) = \langle \phi(t,\tau) \rangle = 1/T \int_{1/\varepsilon}^{(1/\varepsilon)+T} \phi(t,\tau) d\tau \tag{14}$$

The symbol $\langle\ \rangle$ corresponds to the averaging operator. A general decomposition of all variables in the constitutive equation is therefore proposed as

$$\phi(t,\tau) = \bar{\phi}(t) + \tilde{\phi}(t,\tau) \tag{15}$$

The bar corresponds to the solution of a set of averaged equations, while the tilde refers to the oscillatory part. Typically the amplitude of the oscillations is a monotonic function of time, and the oscillations vary in both time scales. Therefore it is assumed that the nonperiodic oscillatory part is obtained by the superposition of the monotonically varying amplitude on a periodic cyclic response. The oscillatory part is decomposed multiplicatively and additively as

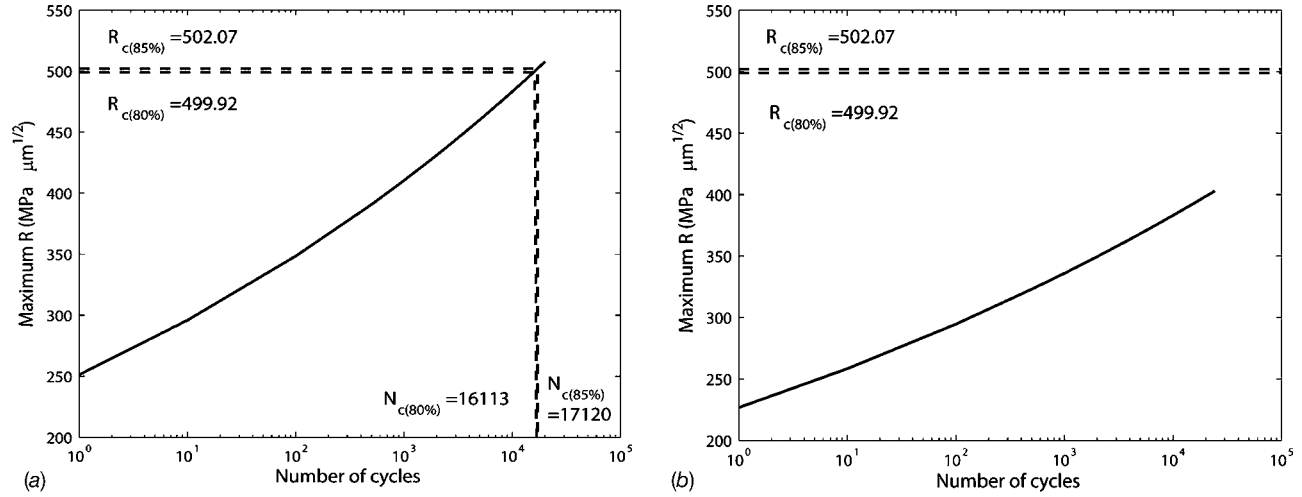

Fig. 10 Evolution of the maximum *R* over the number of cycles for (*a*) dwell fatigue simulation and (*b*) normal fatigue simulation on β forged Ti-6242

$$\tilde{\phi}(t,\tau) = \tilde{\phi}^{\text{nos}}(t,\tau)\tilde{\phi}^{\text{per}}(\tau) = \tilde{\phi}^{\text{osc}}(t,\tau) + \tilde{\phi}^{c}(t) \tag{16}$$

The superscripts "nos" and "per" represent the monotonic and periodic parts of the multiplicative decomposition, respectively. A detailed description of the decomposition of crystal plasticity governing equations in this fashion and obtaining the dual time scale total solution from the superposition of solutions from both time scales is given in Ref. [16]. This technique is employed in the present work to simulate the experiments on β forged Ti-6242 using the microstructure model.

6.3 Calibration of R_c for β Forged Ti-6242. The FE model for β forged Ti-6242 is constructed using the procedure in Sec. 2.2.2 from an OIM scan of a fully β forged Ti-6242 specimen. This specimen had an effective 85% volume fraction of the α phase, the remainder being the β phase [19]. While the field specimens may have been different, the model is for a laboratory specimen of a similar material. A 2 min dwell fatigue simulation is performed on this model for 20,141 cycles with the loading conditions described in Sec. 6.1. Figure 10(*a*) shows the evolution of the maximum R with cycles for this simulation. Following the calibration process in Sec. 4.1, two scenarios of the number of cycles to crack initiation are considered corresponding to 80% and 85% of the total life, i.e., 16,113 cycles and 17,120 cycles. The threshold parameters are determined as $R_{c(80\%)} = 499.92$ MPa$(\mu\text{m})^{1/2}$ and $R_{c(85\%)} = 502.07$ MPa$(\mu\text{m})^{1/2}$ respectively. Comparing with the corresponding calibrated values for α/β forged Ti-6242, it can be seen that the value of R_c for β forged Ti-6242 is higher by $\sim$10%. Therefore, this material has a higher resistance to crack initiation than α/β forged Ti-6242, i.e., it is a tougher material. These calibrated values are used for predicting crack initiation in other experiments on β forged Ti-6242.

6.4 Simulation of the Normal Fatigue Experiment. To predict crack initiation in the normal fatigue experiment using the calibrated values of R_c, a multitime scaling simulation is performed with the FE model for 24,241 cycles (experimental observation). Figure 10(*b*) shows the evolution of the maximum R with cycles for this simulation. It is seen that the maximum R reached at the end of 24,241 cycles is 405.18 MPa$(\mu\text{m})^{1/2}$, which is less than the calibrated values of R_c for the material, i.e., the criterion did not predict crack initiation for this experiment. This inconsistency between the prediction and the experiment leads to the inference that mechanisms in addition to load shedding alone govern failure in the normal fatigue experiment. The crack nucleation criterion is effective only when the predominant mechanism of failure is time dependent load shedding, as evidenced in creep and dwell fatigue.

7 Effect of Macroscopic Loading Conditions on Creep and Dwell Fatigue

For an understanding of the effect of macroscopic loading conditions on creep and dwell fatigue life of Ti-6242, the plastic deformation response is investigated. For these studies the uniform brick mesh with 8000 elements shown in Fig. 9 is used. The model is assigned texture distributions statistically equivalent to the α/β forged Ti-6242 sample [6]. The trend of variation in plastic strain evolution and the local maximum stress at a given time in each simulation are sufficient to provide the relevant information.

7.1 Effect of Loading Constraints on Creep Response of α/β Forged Ti-6242. Three loading cases are considered, viz. equibiaxial tension, uniaxial tension, and tension compression. For the uniaxial case a stress of 800 MPa is applied in the y-direction, for equibiaxial tension a stress of 800 MPa is applied in y- and z-directions, while for the tension-compression case a stress of 800 MPa is applied in the y-direction and a stress of -200 MPa in the z-direction. For each loading case a creep simulation is run for 10,000 s, and the macroscopic plastic strain accumulation over time is plotted in Fig. 11(*a*). The rate of plastic strain accumulation is seen to be lowest for biaxial tension and highest for tension compression. To explain this behavior, a stress triaxiality quotient $q = \sigma_e/(\sqrt{3}\sigma_m)$ is used, where σ_m is the hydrostatic stress and σ_e is the von Mises stress. From this definition, a low value of q indicates a high degree of stress triaxiality. For biaxial tension $q = \sqrt{3}/2$, for uniaxial tension $q = \sqrt{3}$, while for tension compression $q \sim 3\sqrt{3}/2$. Since the hydrostatic component of the applied stress does not contribute to plastic strains, it is obvious that a loading with a high level of stress triaxiality will result in a slower plastic strain accumulation. This explains the plots in Fig. 11(*a*). The implications of this behavior on the local stress levels are studied by plotting the local maximum equivalent stress at 10,000 s against the applied q in Fig. 11(*b*). It is seen that the biaxial loading results in lowest local stress levels, while it is the highest for tension compression. Thus, it may be concluded that a higher triaxiality in applied loading curbs the local load shedding mechanism.

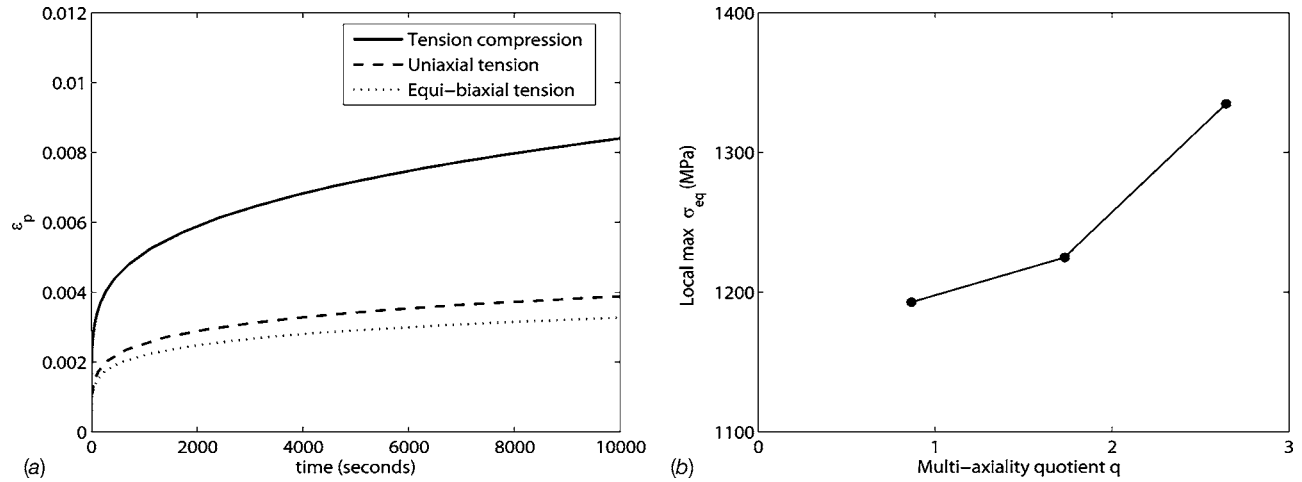

Fig. 11 Effect of loading constraints on (*a*) plastic strain accumulation and (*b*) local maximum equivalent stress at the end of a creep simulation for 10,000 s

7.2 Effect of Hold Time and Stress Ratio on Dwell Fatigue Response. The dwell fatigue life of Ti-6242 is seen to depend on dwell loading parameters such as the hold time and stress ratio [6]. To study the effect of hold time, dwell fatigue simulations are run with the FE model for 100 cycles with different hold times, viz. 1 s, 2 min, and 5 min. For these simulations, the stress ratio is kept at +0.1, and the applied peak load is 869 MPa (95% of the macroscopic yield stress). Plastic strain accumulation per cycle is plotted for each case in Fig. 12(*a*). For a higher hold time, the macroscopic plastic strain accumulation is higher. Correspondingly, the local maximum σ_{22} at the end of 100 cycles also is higher for a high hold time, as seen in Fig. 12(*b*). These results are a consequence of the fact that longer hold times cause more local plastic deformation per cycle, causing more load shedding per cycle. To study the effect of stress ratio, dwell fatigue simulations are run for stress ratios −0.3, 0, and +0.3. The hold time is fixed at 2 min and the peak load at 869 MPa. From Fig. 13(*a*) it can be seen that the plastic strain accumulation per cycle slightly decreases as the stress ratio is made negative. The maximum local σ_{22} at the end of 100 cycles also is lower for negative stress ratio, as shown in Fig. 13(*b*). Therefore a negative stress ratio tends to improve the dwell fatigue life. These studies emphasize that macroscopic loading variables can affect the dwell fatigue life of Ti-6242, desirable conditions being negative stress ratios, lower hold times, and high stress triaxiality in the applied loading.

8 Conclusions

This paper presents the development of a microstructure sensitive crack nucleation criterion in polycrystalline alloy Ti-6242 under dwell fatigue. An experimentally validated rate and size dependent crystal plasticity model is used for the computational modeling of the grain-level mechanical response. The 3D FE models employed consist of statistically equivalent representations of vital microstructural characteristics of a failure site of the Ti-6242 specimen. It is proposed that dwell fatigue crack initiates due to stress concentration caused by the load shedding phenomenon between adjacent hard and soft grains. To predict load shedding induced crack initiation, a criterion that depends on local effective stresses in the hard grain, as well as the nonlocal plastic strains and strain gradients in adjacent soft grains, is proposed. The functional form of the criterion is motivated from the similarities between crack evolution at the tip of a pre-existing crack and a dislocation pileup. It is observed that the local effective stress required to initiate a crack in a hard grain is inversely related to the nonlocal plastic strain and the gradient of plastic strain

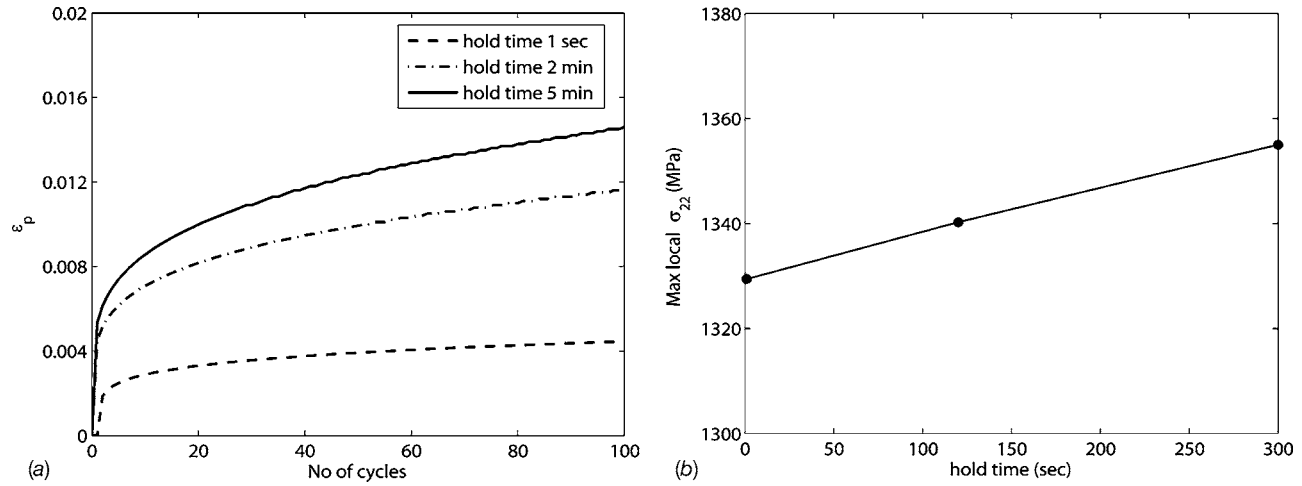

Fig. 12 Effect of hold time on (*a*) plastic strain accumulation by cycle and (*b*) local maximum stress in the loading direction at the end of 100 cycles

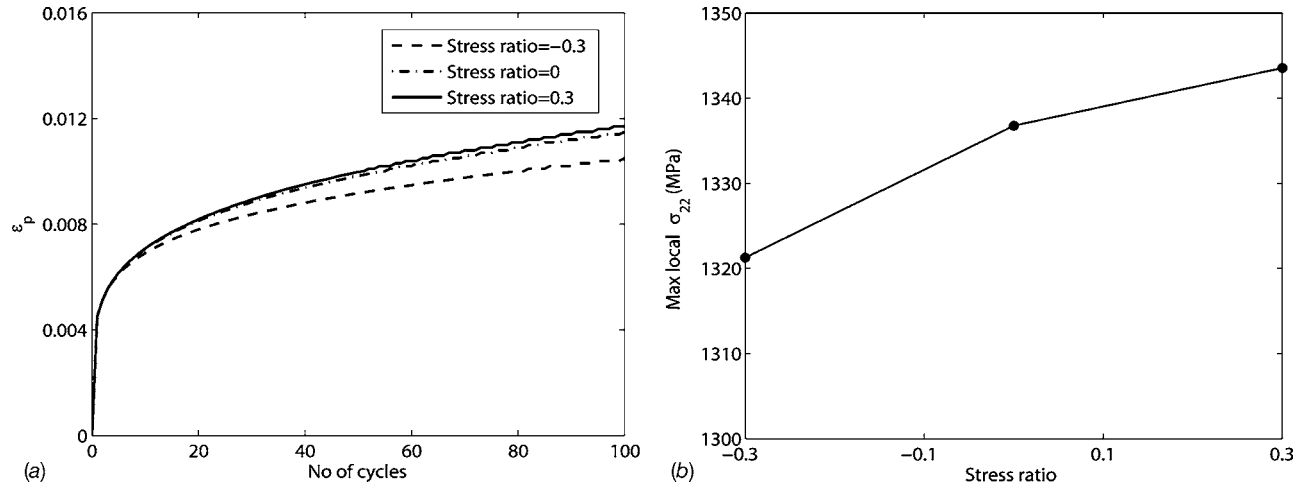

Fig. 13 Effect of stress ratio on (*a*) plastic strain accumulation by cycle and (*b*) local maximum stress in the loading direction at the end of 100 cycles

in the neighboring soft grain. This follows from its inverse square root relation with the dislocation pileup length. The critical material constants in the crack nucleation criterion are calibrated using the experimental results of ultrasonic monitoring of crack evolution in dwell fatigue experiments. The calibrated criterion is successfully validated through accurate predictions of the number of cycles to failure as well as the critical features of the failure site in dwell fatigue experiments. Furthermore, the predictions of the number of cycles to crack initiation for a few critical microstructural features are found to be consistent with previous observations, thus establishing the sensitivity of the criterion to microstructural conditions.

Dwell fatigue studies on β forged Ti-6242 show that this material is stronger than the α/β Ti-6242, with a higher resistance for crack initiation. However, the predicted results also emphasize the existence of failure mechanisms, other than the load shedding, in normal fatigue. The proposed criterion works only if the dominant failure mechanism is load shedding in the polycrystalline microstructure. In Sec. 7, the effect of macroscopic loading conditions on the dwell fatigue response of Ti-6242 is studied. Desirable loading conditions that emerge from these studies are shorter hold times, negative stress ratios, and high stress triaxiality in the applied loading.

The significance of the criterion proposed in this paper is its sensitivity to microstructure. It should be considered as an important first step in the direction of elimination of empiricism in fatigue life prediction. There is some nonuniqueness in the estimation of the length of dislocation pileup at the grain boundary. One can get an estimate of the dislocation pileup length in this context by different ways; Eq. (5) is a direct analytical expression for the dislocation pileup length in terms of the density function per unit length based on single slip system activity. Since this formulation does not directly yield $\rho^l(x)$, we have tried to connect this to the total dislocation density per unit area $\rho^A(x)$ based on a multislip system. $\rho^A(x)$ on the other hand can be derived from the crystal plasticity variables using SSD and GND contributions from the plastic strain and its derivatives. We understand that this is a round about way of connecting the two definitions. To establish this connection, we have assumed that the dislocation pileup for $\rho^A(x)$ follows the same distribution function as that for single slip $\rho^l(x)$ in Eq. (8). The dislocation density per unit length is obtained by multiplying the dislocation density per unit area by a dislocation line width. Thus an assumption made is that the variation in $\rho(x)$ in the direction perpendicular to the distance from the grain boundary is negligible. We realize that there are several assumptions made that could add error to the solution.

There are other possibilities in terms of the evaluation of the pileup length that are currently being investigated. One method uses the slope in the GNDs that can be obtained from $\rho^A(x)$. The authors are currently working on this method. Another alternative is to change the crystal plasticity formulation to one in which the dislocation densities are used directly as variables. This would increase the computations significantly, but the pileup would be a direct outcome of these FEM calculations.

Acknowledgment

The authors are grateful to Professor Jim Williams, Professor Mike Mills, Professor Stan Rokhlin, and Dr. Bahman Zoofan for providing guidance and the experimental data. This work has been supported by the Federal Aviation Administration through Grant No. DTFA03-01-C-0019 (Program Director: Dr. Joe Wilson). This support is gratefully acknowledged. The authors acknowledge the insightful suggestions of Dr. A. Woodfield, Dr. B. Kalb, Dr. A. Chatterjee, Dr. J. Hall, Dr. J. Schirra, Dr. D. Nissley, Dr. A. Walker, and Dr. R. Corran on various aspects of this work. Computer support by the Ohio Supercomputer Center through Grant No. PAS813-2 is also acknowledged.

References

[1] Sinha, V., Mills, M. J., and Williams, J. C., 2004, "Understanding the Contributions of Normal Fatigue and Static Loading to the Dwell Fatigue in a Near-Alpha Titanium Alloy," Metall. Trans. A, **35**, pp. 3141–3148.
[2] Inman, M. A., and Gilmore, C. M., 1979, "Room Temperature Creep of Ti-6Al-4V," Metall. Trans. A, **10A**, pp. 419–425.
[3] Hasija, V., Ghosh, S., Mills, M. J., and Joseph, D. S., 2003, "Modeling Deformation and Creep in Ti-6Al Alloys With Experimental Validation," Acta Mater., **51**, pp. 4533–4549.
[4] Bache, M. R., 2003, "A Review of Dwell Sensitive Fatigue in Titanium Alloys: The Role of Microstructure, Texture and Operating Conditions," Int. J. Fatigue, **25**, pp. 1079–1087.
[5] Woodfield, A. P., Gorman, M. D., Corderman, R. R., Sutliff, J. A., and Yamron, B., 1995, "Effect of Microstructure on Dwell Fatigue Behaviour of Ti-6242," Titanium '95 Science and Technology, The Minerals, Metals and Materials Society, Warrendale, PA, pp. 1116–1124.
[6] Rokhlin, S., Kim, J. Y., and Zoofan, B., 2005, unpublished.
[7] Deka, D., Joseph, D. S., Ghosh, S., and Mills, M. J., 2006, "Crystal Plasticity Modeling of Deformation and Creep in Polycrystalline Ti-6242," Metall. Mater. Trans. A, **37**, pp. 1371–1388.
[8] Venkataramani, G., Deka, D., and Ghosh, S., 2006, "Crystal Plasticity Based FE Model for Understanding Microstructural Effects on Creep and Dwell Fatigue in Ti-6242," ASME J. Eng. Mater. Technol., **128**, pp. 356–365.
[9] Venkatramani, G., Ghosh, S., and Mills, M. J., 2007, "A Size Dependent Crystal Plasticity Finite Element Model for Creep and Load-Shedding in Polycrystalline Titanium Alloys," Acta Mater., **55**, pp. 3971–3986.
[10] Ghosh, S., Bhandari, Y., and Groeber, M., 2008, "CAD Based Reconstruction of Three Dimensional Polycrystalline Microstructures From FIB Generated Serial Sections," Comput.-Aided Des., **40**(3), pp. 293–310.

[11] Groeber, M., Ghosh, S., Uchic, M. D., and Dimiduk, D. M., 2008, "A Framework for Automated Analysis and Representation of 3D Polycrystalline Microstructures, Part 2: Synthetic Structure Generation," Acta Mater., **56**(6), pp. 1274–1287.
[12] Groeber, M. A., 2007, "Development of an Automated Characterization-Representation Framework for the Modeling of Polycrystalline Materials in 3D," Ph.D. thesis, Ohio State University, Columbus, OH.
[13] Stroh, A. N., 1954, "The Formation of Cracks as a Result of Plastic Flow," Proc. R. Soc. London, Ser. A, **223**, pp. 404–414.
[14] Gao, Q., and Liu, H. W., 1990, "Characterization of the Tip Field of a Discrete Dislocation Pileup for the Development of Physically Based Micromechanics," Metall. Trans. A, **21**, pp. 2087–2089.
[15] Hall J., 2006, "Cold Dwell Fatigue Debit in Ti-6242: Honeywell Approach," Honeywell ES&S, unpublished.
[16] Manchiraju, S., Asai, M., and Ghosh, S., 2007, "A Dual-Time-Scale Finite Element Model for Simulating Cyclic Deformation of Polycrystalline Alloys," J. Strain Anal. Eng. Des., **42**, pp. 183–200.
[17] Sinha, V., Mills, M. J., and Williams, J. C., 2006, "Crystallography of Fracture Facets in a Near Alpha Titanium Alloy," Metall. Mater. Trans. A, **37**, pp. 2015–2026.
[18] Sinha, V., Spowart, J. E., Mills, M. J., and Williams, J. C., 2006, "Observations on the Faceted Initiation Site in the Dwell-Fatigue Tested Ti-6242 Alloy: Crystallographic Orientation and Size Effects," Metall. Mater. Trans. A, **37**, pp. 1507–1518.
[19] Williams, J. C., Ghosh, S., Mills, M. J., and Rokhlin, S., 2006, "The Evaluation of Cold Dwell Fatigue in Ti-6242," FAA Report Summary.
[20] Venkataramani, G., Kirane, K., and Ghosh, S., 2008, "Microstructural Parameters Affecting Creep Induced Load Shedding in Ti-6242 by a Size Dependent Crystal Plasticity FE Model," Int. J. Plast., **24**, pp. 428–454.
[21] Suresh, S., 1991, *Fatigue of Materials*, Cambridge University Press, Cambridge, UK.
[22] Baker, I., 1999, "Improving the Ductility of Intermetallic Compounds by Particle-Induced Slip Homogenization," Scr. Mater., **41**(4), pp. 409–414.
[23] Smith, E., 1979, "Dislocations and Cracks," *Dislocations in Solids*, F. R. N. Nabarro, ed., North Holland, Amsterdam, The Netherlands.
[24] Tanaka, K., and Mura, T., 1981, "A Dislocation Model for Fatigue Crack Initiation," ASME J. Appl. Mech., **48**, pp. 97–103.
[25] Griffith A.A., 1920, "The Phenomena of Rupture and Flow in Solids," Philos. Trans. R. Soc. London, Ser. A, **221**, pp. 163–198.
[26] Ruiz, G., Pandolfi, A., and Ortiz, M., 2001, "Three-Dimensional Cohesive Modeling of Dynamic Mixed Mode Fracture," Int. J. Numer. Methods Eng., **52**, pp. 97–120.
[27] Camacho, G. T., and Ortiz, M., 1996, "Computational Modeling of Impact Damage in Brittle Materials," Int. J. Solids Struct., **33**(20–22), pp. 2899–2938.
[28] Parvatareddy, H., and Dillard, D. A., 1999, ""Effect of Mode-Mixity on the Fracture Toughness of Ti-6Al-4V/FM-5 Adhesive Joints," Int. J. Fract., **96**, pp. 215–228.
[29] Lardner, R. W., 1974, *Mathematical Theory of Dislocations and Fracture*, University of Toronto Press, Toronto, Canada.
[30] Huang, Y., Qu, S., Hwang, K. C., Li, M., and Gao, H., 2004, "A Conventional Theory of Mechanism-Based Strain Gradient Plasticity," Int. J. Plast., **20**, pp. 753–782.
[31] Fleck, N. A., and Hutchinson, J. W., 1993, "A Phenomenological Theory for Strain Gradient Effects in Plasticity," J. Mech. Phys. Solids, **41**(12), pp. 1825–1857.
[32] Gao, H., Huang, Y., Nix, W. D., and Hutchinson, J. W., 1999, "Mechanism-Based Strain Gradient Plasticity—I: Theory," J. Mech. Phys. Solids, **47**(6), pp. 1239–1263.
[33] Neeraj, T., Hou, D. H., Daehn, G. S., and Mills, M. J., 2000, "Phenomenological and Microstructural Analysis of Room Temperature Creep in Titanium Alloys," Acta Mater., **48**, pp. 1225–1238.
[34] Engelen, R. A. B., Geers, M. G. D., and Baaijens, F. P. T., 2003, "Nonlocal Implicit Gradient-Enhanced Elasto-Plasticity for the Modeling of Softening Behavior," Int. J. Plast., **19**, pp. 403–433.
[35] Odegard, B. C., and Thompson, A. W., 1974, "Low Temperature Creep of Ti-6Al-4V," Metall. Trans., **5**, pp. 1207–1213.